Geophysical Journal International

Geophys. J. Int. (2026) **246,** 1–19
Advance Access publication 2026 May 8
Research paper

https://doi.org/10.1093/gji/ggag170

ODFTEX: a continuum model for texture evolution with dynamic recrystallization

Neil M. Ribe [1] Manuele Faccenda [2,3] and Brandon VanderBeek [4]

[1] *Laboratoire FAST, Université Paris-Saclay, CNRS, F-91405 Orsay, France. E-mail: neil.ribe@universite-paris-saclay.fr*
[2] *Università degli studi di Padova, Dipartimento di Geoscienze, I-35131 Padova, Italy*
[3] *Istituto Nazionale di Geofisica e Vulcanologia, Sezione di Bologna, I-40127 Bologna, Italy*
[4] *Department of Earth Sciences, University of Oxford, Oxford OX1 3AN, UK*

Accepted 2026 May 4. Received 2026 April 30; in original form 2025 December 23

SUMMARY

We present a new method, ODFTEX, for calculating evolving crystal preferred orientation (CPO) in deforming aggregates of olivine plus orthopyroxene undergoing dynamic recrystallization. The model is based on a continuum description of texture in terms of the orientation distribution function (ODF), which satisfies an evolution equation that we solve numerically. The model thus delivers the ODF directly, rather than a collection of grain orientations like most alternative models. Recrystallization is represented by a source term in the evolution equation, defined in such a way that crystals poorly oriented for slip recrystallize most rapidly. The model has only a single free parameter, the recrystallization rate, which we calibrate against a laboratory experiment on an olivine aggregate deformed in simple shear. We illustrate the predictive power of ODFTEX by using it to calculate evolving CPO along pathlines in a 2-D convective flow and a 3-D subduction zone flow. ODFTEX is computationally about six to seven times faster than the D-Rex model of E. Kaminski *et al.*

Key words: Seismic anisotropy.

1 INTRODUCTION

The primary minerals of the Earth's uppermost mantle, olivine and orthopyroxene, have strongly anisotropic elastic properties. If the crystals of these minerals in a sample of mantle rock are oriented randomly, the rock's bulk elastic properties will be isotropic. If on the contrary the crystals have a non-random orientation distribution (crystallographic preferred orientation or CPO), the speed of an elastic wave traversing the rock will depend on the propagation direction. This 'seismic anisotropy' manifests itself in several observable phenomena, including shear wave birefringence (splitting), azimuthal variation of surface wave speeds and differences in propagation speed between surface waves with different polarizations, that is, Rayleigh and Love waves (J.P. Montagner & L. Guillot 2002; M.D. Long & T.W. Becker 2010).

CPO in the upper mantle is caused principally by progressive deformation of rocks as they participate in the global convective circulation. Under certain conditions of stress, temperature and grain size, olivine and orthopyroxene crystals deform by dislocation creep, a mechanism whereby internal dislocations move through the crystal along a limited number of pairs of crystallographic planes and directions, called slip systems. Deformation by intracrystalline slip constrains the crystallographic axes of individual crystals to rotate relative to a fixed external reference frame, just as a row of tilted books on a shelf rotates when one pushes down on it. Because crystals with different orientations rotate at different rates, an initially isotropic aggregate will quickly develop a non-random CPO. How the overall distribution of orientations evolves with time depends on the geometry of the slip systems and the character of the externally imposed deformation.

The intimate link between deformation, CPO and seismic anisotropy implies that observations of anisotropy can help to constrain the pattern of mantle flow. For this, however, we need a polycrystal mechanics model that can predict quantitatively how CPO evolves during progressive deformation. Several classes of such models exist in the literature.

The models with the highest degree of complexity and physical realism are the so-called full-field models. In these, a polycrystal is treated as an extended array of contiguous grains, and the stress and strain within them are continuous field variables. Numerical solutions can be obtained using either the finite-element method (G.B. Sarma & P.R. Dawson 1996) or the fast Fourier transform (H. Moulinec & P. Suquet 1998; R.A. Lebensohn 2001). However, the high computational cost of full-field models makes them unsuitable for use in convection calculations.

Next in order of decreasing complexity are mean-field homogenization models, often called 'self-consistent' models. In these, the spatial distribution of the grains is ignored and the aggregate is treated as a finite number of coexisting mechanical phases with different orientations and (possibly) material properties. Compatibility of stress and strain is enforced between each phase and a homogeneous effective medium defined by the average of all the other phases. The best-known model in this class is the viscoplastic self-consistent (VPSC) model (A. Molinari *et al.* 1987; R.A. Lebensohn & C.N. Tomé 1993), which has been widely used in geodynamics (H.R. Wenk *et al.* 1991; A. Tommasi 1998; Z.H. Li *et al.* 2014). A more accurate variant of the homogenization approach is the second-order self-consistent (SOSC) model (P. Ponte Castañeda 2002; Y. Liu & P. Ponte Castañeda 2004). Comparisons of full-field and homogenization models have been done by R.A. Lebensohn *et al.* (2004a, b, 2011) and (for olivine) by O. Castelnau *et al.* (2008).

Still simpler are models of the 'kinematical' class, which are based on expressions for the deformation-induced rate of crystallographic rotation as a function of grain orientation. Examples of such models include N.M. Ribe & Y. Yu (1991) and the D-Rex model of E. Kaminski & N. Ribe (2001) and E. Kaminski *et al.* (2004), which has been widely used to predict CPO and seismic anisotropy in upper mantle flow models (T.M. Lassak *et al.* 2006; J.A. Conder & D.A. Wiens 2007; T.W. Becker *et al.* 2008; M. Faccenda & F.A. Capitanio 2013). An alternative kinematical model that matches the predictions of the SOSC model nearly exactly is the ANPAR model of N. Goulding *et al.* (2015). Kinematical models are computationally $\approx 10^4$ times faster than homogenization models.

A further degree of computational and physical simplicity is represented by 'director' models (H. Mühlhaus *et al.* 2002; H.B. Mühlhaus *et al.* 2004). Here one represents anisotropy by the orientation of one or more lines or 'directors' that are advected, rotated and stretched by the flow. E. Lev & B.H. Hager (2008) used a model with 40 directors to approximate continuous orientation distributions. L.N. Hansen *et al.* (2016) and A. Király *et al.* (2020) proposed a modified director method (MDM) in which the driving force for rotation depends on the orientation of the director (the Burgers vector) relative to the flow. N. Rathmann *et al.* (2024) proposed a spectral directors method (SDM) in which continuous distributions of directors are approximated by truncated spherical harmonic expansions.

The final and simplest approach to modelling textural evolution is to follow the evolution of the finite strain ellipsoid (FSE) along pathlines in the flow. This approach is based on the suggestion of D. McKenzie (1979) that CPO depends only on the finite strain experienced by the rock, and is independent of the details of the deformation history. For olivine with relative slip system strengths corresponding to an A-type fabric (H. Jung *et al.* 2006), the finite-strain hypothesis states that the a and b crystallographic axes are concentrated around the longest and shortest axes of the FSE, respectively. This hypothesis has been used in a variety of numerical modelling studies (J. Phipps Morgan 1987; P.G. Silver & W.W. Chan 1991; N.M. Ribe 1992; C.E. Hall *et al.* 2000; D.K. Blackman & J.M. Kendall 2002; M.D. Long *et al.* 2007; Z.H. Li *et al.* 2014; N.M. Ribe *et al.* 2019).

In this paper we propose a new kinematical model, ODFTEX, that differs from previous models in two principal ways. First, ODFTEX is based on a continuum description of CPO, rather than a discrete representation in terms of a large number (typically a few thousand) of individual grains. A discrete representation is used in most common texture evolution models, including VPSC, SOSC D-Rex and MDM. In contrast, ODFTEX is based on solving an evolution equation for the orientation distribution function (ODF), which is a continuous function of the three Eulerian angles that describe the orientations of crystals relative to an external reference frame. Because the model delivers the ODF directly, it is not necessary to reconstruct it (by a necessarily non-unique procedure) from a collection of individual crystal orientations.

The second novel aspect of ODFTEX is a new parametrization of dynamic recrystallization that is compatible with the model's continuum framework. The need to account for dynamic recrystallization arises from the fact that the finite-strain hypothesis of D. McKenzie (1979) is called into question by laboratory experiments. S. Zhang & S.I. Karato (1995) deformed aggregates of olivine crystals in simple shear, and measured the peak orientation of the [100] axis as a function of shear strain. They found that the [100] peak rotated toward the shear plane much faster than did the long axis of the FSE. This result implies that a mechanism in addition to pure intracrystalline slip, namely dynamic recrystallization, was operative in their experiments.

A number of texture evolution models including dynamic recrystallization already exist in the literature. A. Etchecopar & G. Vasseur (1987) proposed a 3-D geometrical model based on the minimization of gaps, overlaps and boundary displacements between neighbouring deforming grains. Recrystallization was modelled by assuming that grains revert to the shapes and orientations they had at the previous deformation step if the post-minimization gaps and overlaps are too large. H.R. Wenk & C.N. Tomé (1999) proposed a model in which recrystallization is governed by a balance of grain-boundary migration (growth of relatively undeformed grains) and nucleation of strain-free nuclei replacing highly deformed grains. The parameters of the model are a grain-growth parameter C, an energy normalization factor E_0, an initial threshold stress τ_0^s in the absence of dislocations, a threshold percentage B_1 of the maximum strain increment required for nucleation, a nucleation rate parameter B_2 and a critical size B_3 above which a nucleus recombines with its parent grain. D-Rex (E. Kaminski *et al.* 2004) includes a recrystallization model that is also based on a description of microscopic mechanisms. It involves three dimensionless parameters: a grain boundary mobility M^*, a nucleation rate λ^* of dislocation-free subgrains and a critical grain size reduction factor χ below which grains deform by grain-boundary sliding. Finally, J. Signorelli & A. Tommasi (2015) proposed a model for recrystallization by subgrain rotation. Its free parameters are a threshold strain ε_0 above which subgrains form, a subgrain nucleation efficiency E_2, a maximum number n of subgrains into which a grain can fragment, a reference strain increment $\Delta\epsilon_{ref}$ and a maximum possible subgrain misorientation ϑ_0.

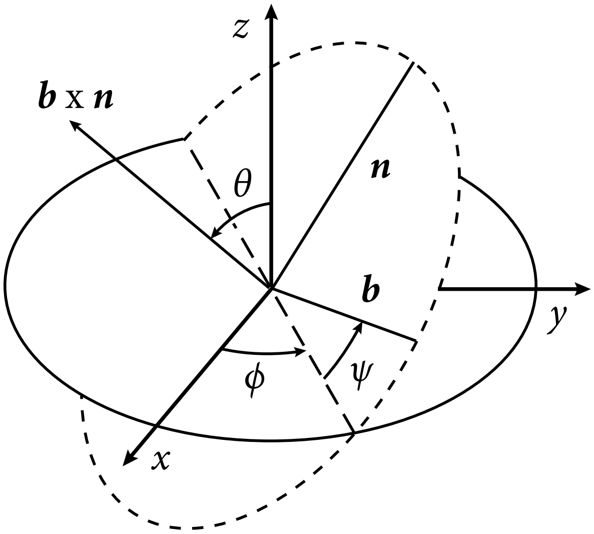

Figure 1. General definition of the Eulerian angles relative to the slip direction $\boldsymbol{b}$ and the normal vector to the slip plane $\boldsymbol{n}$.

This study takes a different approach. Instead of attempting to specify the complicated microscopic mechanisms of dynamic recrystallization, we employ the simple hypothesis that crystals poorly oriented for slip gradually disappear while well-oriented crystals grow. The resulting quantitative model has only a single free parameter, a recrystallization rate with dimensions of inverse time. By adjusting this parameter, we are able to get remarkably good fits to laboratory textures observed by K.H. Lee *et al.* (2002) for deformation by simple shear and A. Nicolas *et al.* (1973) for uniaxial compression.

Our study is organized as follows. In Section 2, we review the Eulerian angles $(\phi, \theta, \psi) \equiv \mathbf{g}$ that describe the orientations of individual crystals and the orientation distribution function $f(\mathbf{g}, t)$ that describes distributions of those orientations. In Section 3 we use a simple minimization principle to determine the orientation-dependent crystallographic spin $\dot{\mathbf{g}}(\mathbf{g})$ of a crystal with a single slip system in response to an externally imposed triaxial straining deformation. In Section 4 we introduce our evolution equation for $f(\mathbf{g}, t)$, which includes an inhomogeneous term that represents dynamic recrystallization. In Section 5 we specialize the evolution equation to plane strain deformations with arbitrary vorticity. By comparing solutions of this equation to the simple shear texture obtained experimentally by K.H. Lee *et al.* (2002), we estimate the recrystallization rate parameter of our dynamic recrystallization model. In Section 6 we show that the same recrystallization rate parameter also gives an excellent fit to a texture observed experimentally under uniaxial compression (A. Nicolas *et al.* 1973). In Section 7.1 we solve the evolution equation along pathlines in a 2-D convective flow, and in Section 7.2 we do the same for a model of the 3-D flow around a subducting slab. Finally, Section 8 is a discussion and summary of our results.

2 CRYSTAL ORIENTATION AND ORIENTATION DISTRIBUTIONS

Consider a polycrystal composed of a large number of crystals of olivine (volume fraction $1 - \Delta$) and orthopyroxene (volume fraction Δ). We suppose that each olivine crystal has only one active slip system, which may be (010)[100], (001)[100] or (010)[001], and that each orthopyroxene crystal has the single active slip system (100)[001] (S.I. Karato *et al.* 2008). Let $\boldsymbol{b}$ and $\boldsymbol{n}$ be vectors in the slip direction and normal to the slip plane, respectively, for any of these four slip systems. Table 1 lists and defines the symbols used in this section and the following ones.

The orientation of the crystallographic axes of a crystal relative to fixed external axes can be specified by three Eulerian angles $(\phi, \theta, \psi) \equiv \mathbf{g}$. Fig. 1 shows the angles we use. Instead of defining these angles with respect to the crystallographic axes [100], [010] and [001], we define them relative to the slip direction $\boldsymbol{b}$, the normal vector $\boldsymbol{n}$ and the vector $\boldsymbol{b} \times \boldsymbol{n}$. The reason for this is that intracrystalline slip is a simple shear in the $\boldsymbol{b}$-$\boldsymbol{n}$ plane, which corresponds to a crystallographic spin that is parallel to $\boldsymbol{b} \times \boldsymbol{n}$, with no components in the $\boldsymbol{b}$- or $\boldsymbol{n}$-directions. Thus when the Eulerian angles are defined as in Fig. 1, intracrystalline slip changes only the crystal's Eulerian angle ψ, and not the angles ϕ or θ. For crystals with orthorhombic symmetry such as olivine and orthopyroxene, the ranges of the Eulerian angles are $\phi \in [0, \pi]$, $\theta \in [0, \pi]$ and $\psi \in [0, \pi]$.

Fig. 2 shows how the directions $\boldsymbol{b}$, $\boldsymbol{n}$ and $\boldsymbol{b} \times \boldsymbol{n}$ are related to the crystallographic axes [100], [010] and [001] for each of our four slip systems. To maintain consistency with the right-hand rule, the normal vectors $\boldsymbol{n}^{(2)}$ and $\boldsymbol{n}^{(3)}$ for slip systems $s = 2$ and $s = 3$ must be taken to be [00–1] and [0–10], respectively.

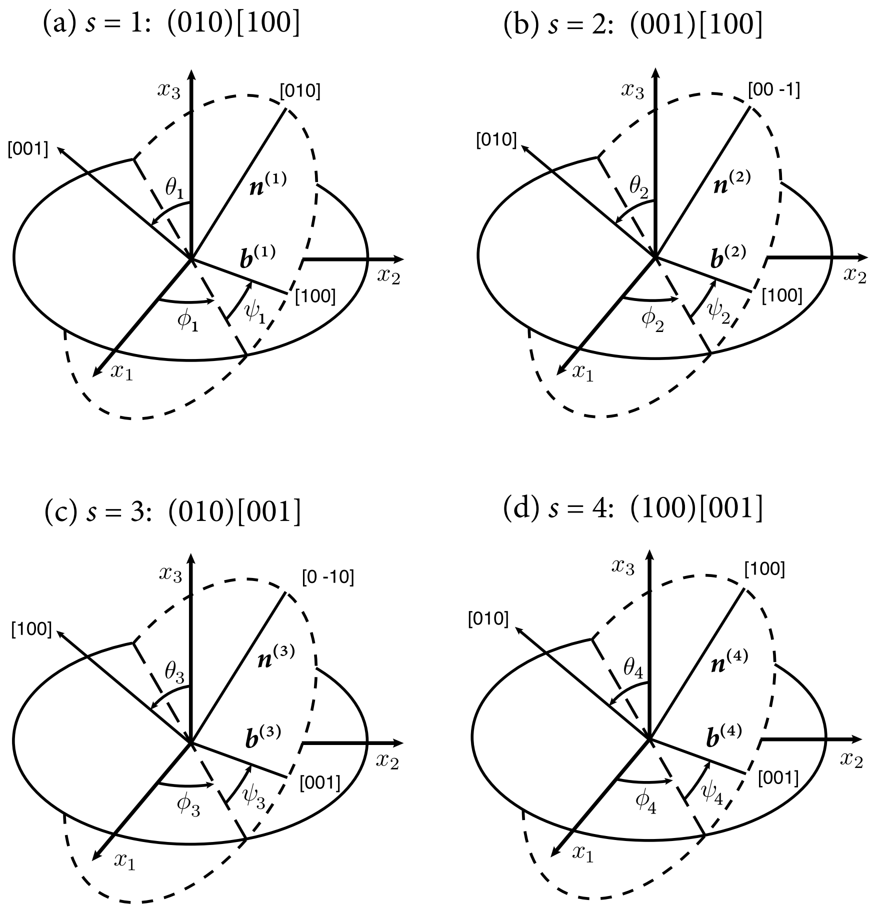
(a) $s = 1$: (010)[100]
(b) $s = 2$: (001)[100]
(c) $s = 3$: (010)[001]
(d) $s = 4$: (100)[001]

Figure 2. Eulerian angles associated with each of the four slip systems $s = 1$–4.

As we proceed, we will take the Eulerian angles $(\phi_1, \theta_1, \psi_1)$ for slip system $s = 1$ to be the standard ones and relate the other sets to these. To this end we seek rotation matrices $\boldsymbol{M}^{(s)}$ $(s = 2, 3, 4)$ such that

$$\boldsymbol{b}^{(s)} = \boldsymbol{M}^{(s)}\boldsymbol{b}^{(1)}, \quad \boldsymbol{n}^{(s)} = \boldsymbol{M}^{(s)}\boldsymbol{n}^{(1)},$$
$$\boldsymbol{b}^{(s)} \times \boldsymbol{n}^{(s)} = \boldsymbol{M}^{(s)}(\boldsymbol{b}^{(1)} \times \boldsymbol{n}^{(1)}). \tag{1}$$

The matrices that satisfy the foregoing relations are

$$\boldsymbol{M}^{(2)} = \begin{pmatrix} 1 & 0 & 0 \\ 0 & 0 & 1 \\ 0 & -1 & 0 \end{pmatrix}, \quad \boldsymbol{M}^{(3)} = \begin{pmatrix} 0 & 0 & 1 \\ 0 & -1 & 0 \\ 1 & 0 & 0 \end{pmatrix}, \quad \boldsymbol{M}^{(4)} = \begin{pmatrix} 0 & 1 & 0 \\ 0 & 0 & 1 \\ 1 & 0 & 0 \end{pmatrix}. \tag{2}$$

The matrix $\boldsymbol{M}^{(1)}$ is simply the identity matrix.

The orientation of the crystallographic axes relative to the sample coordinate system can also be characterized by a matrix $\boldsymbol{a}$ of direction cosines. For generic Eulerian angles $(\phi, \theta, \psi) \equiv \mathbf{g}$, we have

$$\boldsymbol{a} = \begin{pmatrix} \mathrm{c}\phi\,\mathrm{c}\psi - \mathrm{s}\phi\,\mathrm{s}\psi\,\mathrm{c}\theta & \mathrm{s}\phi\,\mathrm{c}\psi + \mathrm{c}\phi\,\mathrm{s}\psi\,\mathrm{c}\theta & \mathrm{s}\psi\,\mathrm{s}\theta \\ -\mathrm{c}\phi\,\mathrm{s}\psi - \mathrm{s}\phi\,\mathrm{c}\psi\,\mathrm{c}\theta & -\mathrm{s}\phi\,\mathrm{s}\psi + \mathrm{c}\phi\,\mathrm{c}\psi\,\mathrm{c}\theta & \mathrm{c}\psi\,\mathrm{s}\theta \\ \mathrm{s}\phi\,\mathrm{s}\theta & -\mathrm{c}\phi\,\mathrm{s}\theta & \mathrm{c}\theta \end{pmatrix}, \tag{3}$$

where c and s indicate the cosine and sine, respectively, of the angle immediately following.

In the limit as the number of grains tends to infinity, the distribution of their orientations can be described by a continuous function f, the ODF. In the case of texture evolution we consider the ODF as a time-dependent function $f(\mathbf{g}, t)$ defined such that $f(\mathbf{g}, t)\mathrm{d}\mathbf{g}$ is the volume fraction of crystals with orientations in an element $\mathrm{d}\mathbf{g}$ of the Euler space centred on $\mathbf{g}$ at time t. With a proper normalization, the ODF of a uniform (random) distribution is $f = 1$. Accordingly, the anisotropic part of an arbitrary ODF f is $f - 1$. Throughout this paper, all ODFs and associated pole figures are expressed as multiples of a random distribution.

The numerical solutions for $f(\mathbf{g}, t)$ described below deliver a 'master' ODF that is a function of the general Eulerian angles shown in Fig. 1. This master ODF must then be transformed to the standard set of Eulerian angles $(\phi_1, \theta_1, \psi_1)$. This is done in three steps. First, one calculates the direction cosine matrix $\boldsymbol{a}$ corresponding to the general Eulerian angles delivered by the numerical solution. Next, one forms the matrix product $\boldsymbol{M}^{(s)}\boldsymbol{a}$ for $s = 1, 2$ or 3 (for olivine) and $s = 4$ (for orthopyroxene, if present). Finally, one determines the Eulerian angles corresponding to $\boldsymbol{M}^{(s)}\boldsymbol{a}$, which become the new arguments of $f(\mathbf{g}, t)$. Of course there is nothing to do for the case $s = 1$, because $\boldsymbol{M}^{(1)}$ is the identity matrix.

3 CRYSTALLOGRAPHIC SPIN

To formulate a description of crystallographic spin, we consider a monomineralic polycrystal in which only a single slip system is active. The unit vectors associated with the slip system are $\boldsymbol{b}$ and $\boldsymbol{n}$, and the Eulerian angles are (ϕ, θ, ψ). The local strain rate tensor within a crystal is

$$e_{ij} = \dot{\gamma} S_{ij}, \quad S_{ij} = \frac{1}{2}(n_i b_j + n_j b_i), \tag{4}$$

where $\dot{\gamma}$ is the slip rate and S_{ij} is the Schmid tensor. To determine the rate of deformation-induced crystallographic spin, we use a simple procedure due to N.M. Ribe & Y. Yu (1991), wherein one minimizes the second invariant $\mathcal{E}$ of the difference between e_{ij} and the global strain rate tensor E_{ij}, viz.

$$\mathcal{E} = (e_{ij} - E_{ij})(e_{ij} - E_{ij}). \tag{5}$$

The shear rate that minimizes $\mathcal{E}$ is

$$\dot{\gamma} = 2E_{ij}S_{ij}. \tag{6}$$

The crystallographic spin associated with the shear, which we shall call the intrinsic spin, is

$$\dot{\boldsymbol{\omega}} = \frac{\dot{\gamma}}{2}\boldsymbol{b} \times \boldsymbol{n}. \tag{7}$$

4 EVOLUTION EQUATION FOR THE ODF

In the absence of recrystallization and extrinsic spin, the time evolution of the ODF is governed by the continuity equation (A. Clement 1982)

$$\begin{aligned} &\frac{\partial f}{\partial t} + \frac{\partial}{\partial \phi}(\dot{\phi} f) + \frac{1}{\sin\theta}\frac{\partial}{\partial\theta}(\dot{\theta}\sin\theta f) + \frac{\partial}{\partial\psi}(\dot{\psi} f) \\ &\equiv \frac{\partial f}{\partial t} + \nabla\cdot(\dot{\mathbf{g}} f) = 0, \end{aligned} \tag{8}$$

where $(\dot{\phi}, \dot{\theta}, \dot{\psi}) \equiv \dot{\mathbf{g}}$ is the intrinsic spin of a crystal and $\nabla\cdot$ is the divergence operator in the space of the Eulerian angles (the 'Euler space'). In general, $\dot{\mathbf{g}}$ depends on the imposed macroscopic strain rate tensor E_{ij}, the crystal's orientation $\mathbf{g}$ and the overall orientation distribution f. Eq. (8) is a conservation law which states that the rate of change of the volume fraction of crystals having orientations in a small element $\mathrm{d}\mathbf{g}$ of the Euler space is equal to the net flux of crystal orientations into this element.

4.1 Modified evolution equation

In this study we use a modified evolution equation obtained by altering (8) in three ways. First, we set $\dot{\phi} = \dot{\theta} = 0$ because $\dot{\psi}$ is the only non-zero component of the intrinsic spin, as discussed in Section 2. Secondly, we add a term $\nabla\cdot(\dot{\mathbf{g}}_e f)$ to the left-hand side, where $\dot{\mathbf{g}}_e$ is the imposed extrinsic spin (one-half the vorticity). This allows us to model rotational deformations such as simple shear. Thirdly, we add to the right-hand side an inhomogeneous recrystallization rate term $f\hat{J}(\mathbf{g})$, where $\hat{J}(\mathbf{g})$ remains to be determined. The hat symbol indicates that $\hat{J}$ is dimensional (units of inverse time). Note that the recrystallization rate of crystals with a given orientation is assumed to be proportional to their relative abundance in the aggregate, measured by f. Our new evolution equation is therefore

$$\frac{\partial f}{\partial t} + \nabla\cdot(\dot{\mathbf{g}}_e f) + \frac{\partial}{\partial\psi}(\dot{\psi} f) = f\hat{J}(\mathbf{g}). \tag{9}$$

The Eulerian components $(\dot{\phi}_e, \dot{\theta}_e, \dot{\psi}_e)$ of the extrinsic spin $\dot{\mathbf{g}}_e$ are related to its Cartesian components $\dot{\Omega}_i$ by

$$\begin{aligned} \dot{\phi}_e &= \dot{\Omega}_3 + \cot\theta(\dot{\Omega}_2\cos\phi - \dot{\Omega}_1\sin\phi) \\ &= |\dot{\boldsymbol{\Omega}}|\left[\cos\theta_e - \cot\theta\sin\theta_e\sin(\phi - \phi_e)\right], \end{aligned} \tag{10a}$$

$$\dot{\theta}_e = \dot{\Omega}_1 \cos\phi + \dot{\Omega}_2 \sin\phi = |\dot{\mathbf{\Omega}}| \sin\theta_e \cos(\phi - \phi_e), \tag{10b}$$

$$\dot{\psi}_e = \csc\theta(\dot{\Omega}_1 \sin\phi - \dot{\Omega}_2 \cos\phi) = |\dot{\mathbf{\Omega}}| \csc\theta \sin\theta_e \sin(\phi - \phi_e), \tag{10c}$$

where (θ_e, ϕ_e) are the spherical coordinates of the unit vector parallel to the extrinsic spin vector $\dot{\mathbf{\Omega}}$.

4.2 Recrystallization model

The first constraint we impose on $\hat{J}(\mathbf{g})$ is

$$\frac{1}{2\pi^2} \int \hat{J}(\mathbf{g}) \mathrm{d}\mathbf{g} = 0, \tag{11}$$

which means that disappearance of crystals with a given orientation is compensated by the appearance of new crystals with some other orientation. However, while $\hat{J}(\mathbf{g})$ has zero mean the product $f\hat{J}(\mathbf{g})$ does not unless $f = 1$. We shall therefore have to normalize our solutions of (9) to ensure that $f(\mathbf{g})$ always has a unit integral over the Euler space.

Next, we assume that crystals tend to disappear by recrystallization if they are unfavourably oriented for slip, that is, if they have a relatively high value of the strain rate misfit $\mathcal{E}$ defined by (5). In other words, we assume that

$$\hat{J} = \hat{J}(\mathcal{E}). \tag{12}$$

An appropriate expression is $J \equiv \hat{J}/\epsilon_0 \propto C - \dot{\epsilon}_0^{-2}\mathcal{E}$ where the dimensionless constant C is chosen so that (11) is satisfied. The negative sign is present because unfavourably oriented crystals tend to disappear. More explicitly,

$$\begin{aligned} J &\propto C - \dot{\epsilon}_0^{-2}\left[(2S_{kl}E_{kl}S_{ij} - E_{ij})(2S_{mn}E_{mn}S_{ij} - E_{ij})\right] \\ &= C - \dot{\epsilon}_0^{-2}\left[E_{ij}E_{ij} - 2(S_{ij}E_{ij})^2\right], \end{aligned} \tag{13}$$

where we have used the identity $S_{ij}S_{ij} = 1/2$ and

$$\dot{\epsilon}_0 = \sqrt{E_{ij}E_{ij}/2} \tag{14}$$

is a characteristic strain rate scale. Now $S_{ij}E_{ij} = \dot{\psi}$. Thus we have

$$\hat{J} \propto C_1 + \frac{2}{\dot{\epsilon}_0^2}\dot{\psi}^2, \tag{15}$$

where $C_1 = C - 2$. Finally, we introduce a constant of proportionality, the recrystallization rate Λ (units s^{-1}). Thus (15) becomes

$$\hat{J} = \Lambda\left(C_1 + \frac{2}{\dot{\epsilon}_0^2}\dot{\psi}^2\right), \tag{16}$$

where

$$\begin{aligned} C_1 &= -\frac{1}{2\pi^2}\int \frac{2}{\dot{\epsilon}_0^2}\dot{\psi}^2 \mathrm{d}\mathbf{g} \\ &= -\frac{2}{5\dot{\epsilon}_0^2}(E_{11}^2 + E_{12}^2 + E_{11}E_{22} + E_{22}^2 + E_{23}^2 + E_{31}^2). \end{aligned} \tag{17}$$

5 EVOLUTION OF TEXTURE UNDER PLANE STRAIN

We begin with the relatively simple case of plane strain with arbitrary extrinsic spin $\dot{\Omega}$ normal to the plane of deformation. We now non-dimensionalize (9) by defining a dimensionless time $\tau = \dot{\epsilon}_0 t$, a dimensionless intrinsic spin $\dot{\Psi} = \dot{\psi}/\dot{\epsilon}_0$, a dimensionless recrystallization rate $\lambda = \Lambda/\dot{\epsilon}_0$ and a dimensionless extrinsic spin (vorticity number) $\Gamma = \dot{\Omega}/\dot{\epsilon}_0$. The evolution equation then takes the dimensionless form

$$\frac{\partial f}{\partial \tau} + \Gamma\frac{\partial f}{\partial \phi} + \frac{\partial}{\partial \psi}(\dot{\Psi} f) = 2\lambda f\left(\dot{\Psi}^2 - \frac{1}{5}\right). \tag{18}$$

For simplicity, we shall assume that Γ is constant and that the Eulerian angles (ϕ, θ, ψ) are measured relative to Cartesian axes aligned with the principal axes of the imposed strain rate tensor E_{ij}.

5.1 Pure shear

Fig. 3 shows textures for a pure olivine aggregate deformed by pure shear ($\Gamma = 0$), obtained by solving (18) numerically using the method of characteristics to a strain $\dot{\epsilon}t = 0.7$. The method of characteristics is a solution method for hyperbolic partial differential equations that accumulates changes in the dependent variable (here the ODF) along curves called characteristics, which in our case are simply the trajectories followed by individual crystal orientations as they ‘wander’ through the Euler orientation space during

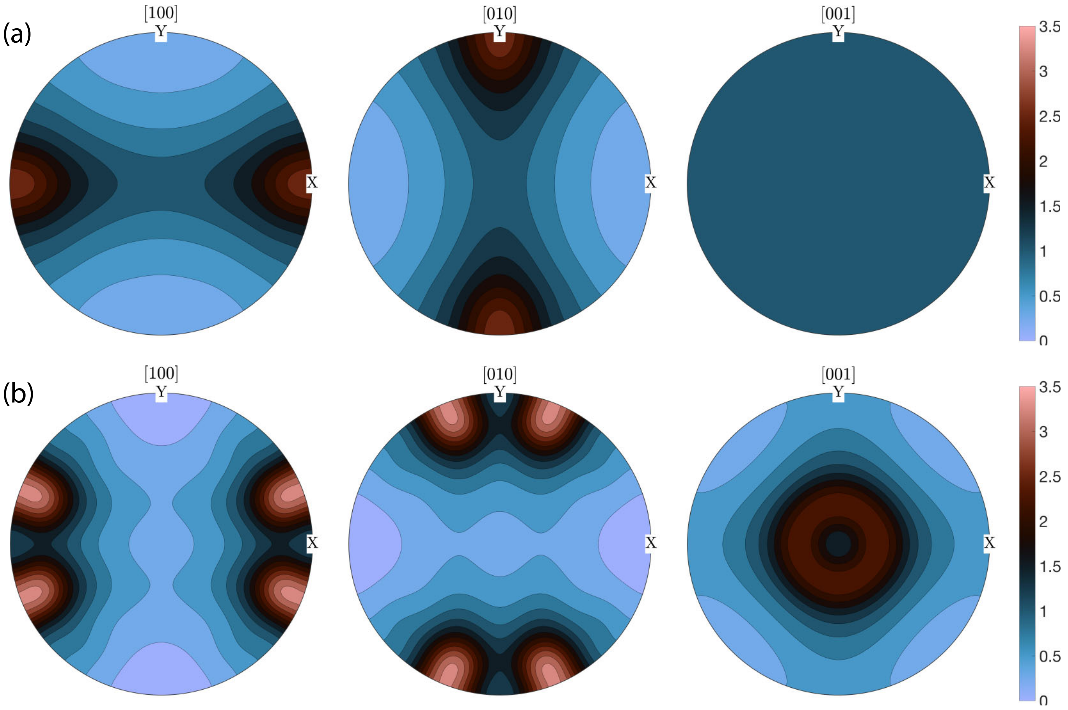

Figure 3. Texture due to deformation of an olivine aggregate under pure shear ($\Gamma = 0$) to a strain $\dot{\epsilon}t = 0.7$. (a) without recrystallization ($\lambda = 0$); (b) with recrystallization ($\lambda = 2.6$). The only active slip system is (010)[100]. The extensional axis is horiziontal.

progressive deformation. In Fig. 3, the extensional axis is horizontal. Results are shown both (a) without and (b) with dynamic recrystallization. A notable feature of Fig.3(a) is that [001] has a random distribution. This is a general feature of textures produced by the activity of a single slip system in the absence of recrystallization, for which the distribution of the $\boldsymbol{b} \times \boldsymbol{n}$ axis is always isotropic (N.M. Ribe *et al.* 2019). At first sight it seems paradoxical that a population of grains having strong concentrations of both [100] and [010] would not at the same time have a strong concentration of the third axis [001]. The resolution of the paradox is that the grains with strongly concentrated [100] are not the same as those with strongly concentrated [010] (R. Hielscher, personal communication.) The net orientational effect of these two distinct grain populations is an isotropic distribution of [001]. The isotropy of the $\boldsymbol{b} \times \boldsymbol{n}$ axis when only one slip system is active and recrystallization is absent is a mathematically exact result, and is independent of both the strength and the symmetry of the preferred orientations of the other two axes. However, we emphasize that an isotropic $\boldsymbol{b} \times \boldsymbol{n}$ distribution is unlikely to be encountered in nature because of the effects of dynamic recrystallization and/or the presence of additional active slip systems.

Turning to Fig. 3(b), we see that recrystallization influences the texture in three ways: it makes it stronger overall; it makes the [001] pole figure anisotropic; and it splits the peaks in the [100] and [010] pole figures. The splitting of the [100] and [010] peaks can be understood by noting that the recrystallization rate term on the right-hand side of eq. (18) depends on the square $\dot{\Psi}^2$ of the spin $\dot{\Psi}$. Because $\dot{\Psi}$ is a generalized spherical harmonic of degree 2, $\dot{\Psi}^2$ is dominantly of degree 4 and has a wavelength one-half that of $\dot{\Psi}$. This degree-4 contribution to the recrystallization rate manifests itself in the appearance of two narrower (degree 4) peaks where only one wider (degree 2) peak was present in the absence of recrystallization.

5.2 Simple shear

Turning now to simple shear ($\Gamma = 1$), we first examine how the texture of a pure olivine polycrystal without recrystallization depends on the strain. Fig. 4 shows the numerically predicted textures for shear strains of (a) 100 per cent ($\tau = 0.5$) and (b) 200 per cent ($\tau = 1.0$). The white lines on the [100] pole figures indicate the orientations of the long axis of the finite strain ellipsoid. The peaks of the [100] orientation follow exactly the orientation of that axis, supporting the hypothesis of D. McKenzie (1979) that texture is a unique function of finite strain when recrystallization is not active.

5.2.1 Calibration against a laboratory experiment

Our next step is to calibrate our model against an experimental texture obtained by deforming an olivine polycrystal in simple shear. We use the data from the MIT23 experiment of K.H. Lee *et al.* (2002), which was carried out at a temperature of 1573 K and a strain rate 9.5×10^{-5} s^{-1} to a total shear strain of 140 per cent ($\tau = 0.7$). The pole figures of the three crystallographic axes are shown in Fig. 5(a).

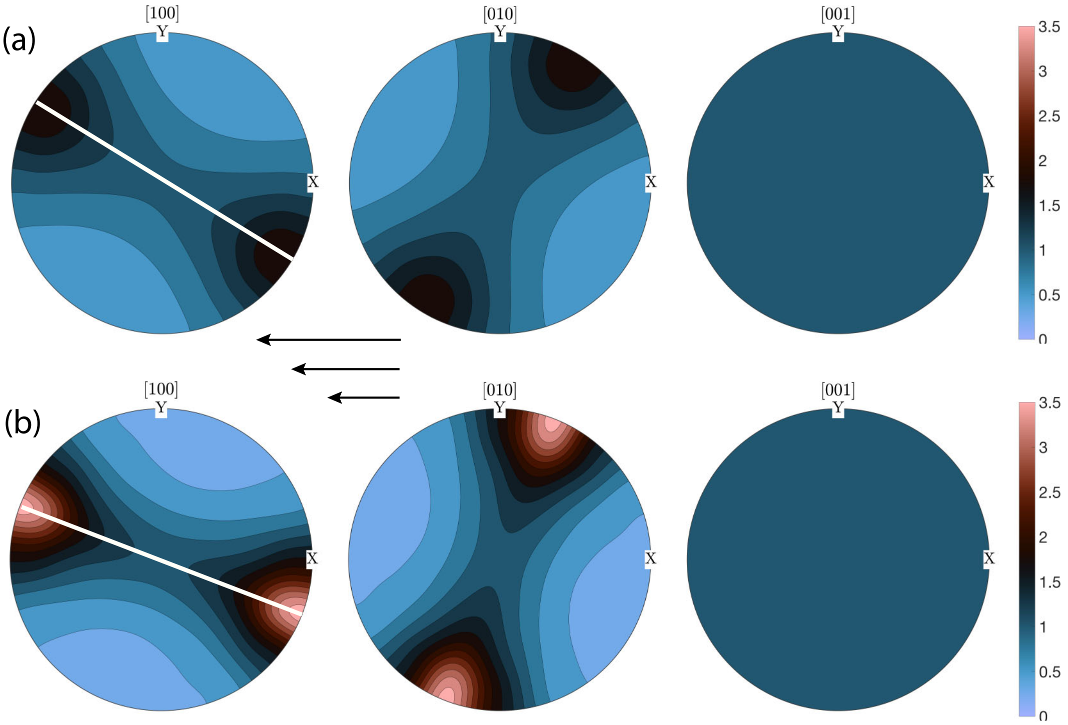

Figure 4. Texture due to deformation of an olivine aggregate under simple shear ($\Gamma = 1$) without recrystallization ($\lambda = 0$). Parts (a) and (b) correspond to shear strains of 100 per cent and 200 per cent, respectively. The only active slip system is (010)[100]. The white lines on the [100] pole figures indicate the orientations of the longest axis of the finite strain ellipsoid.

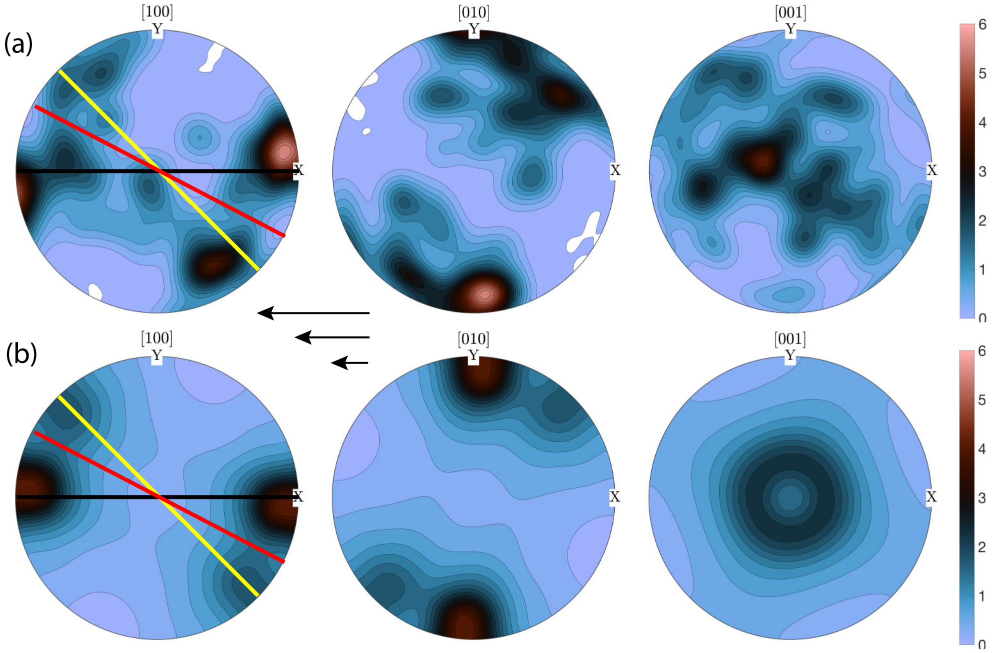

Figure 5. Comparison of model predictions with observations for an olivine aggregate deformed in simple shear to 140 per cent shear strain. (a) Pole figures for sample MIT23 from K.H. Lee *et al.* (2002), with the sense of shear shown just below. Several key directions are indicated on the [100] pole figure: the shear plane (black), the direction of maximum instantaneous extension rate (yellow) and the orientation of the long axis of the finite strain ellipsoid (red). Small white patches on the [100] and [010] pole figures indicate ranges of orientation that are unpopulated by any crystal. (b) Pole figures predicted by ODFTEX for 140 per cent shear strain and a recrystallization rate $\lambda = 2.6$.

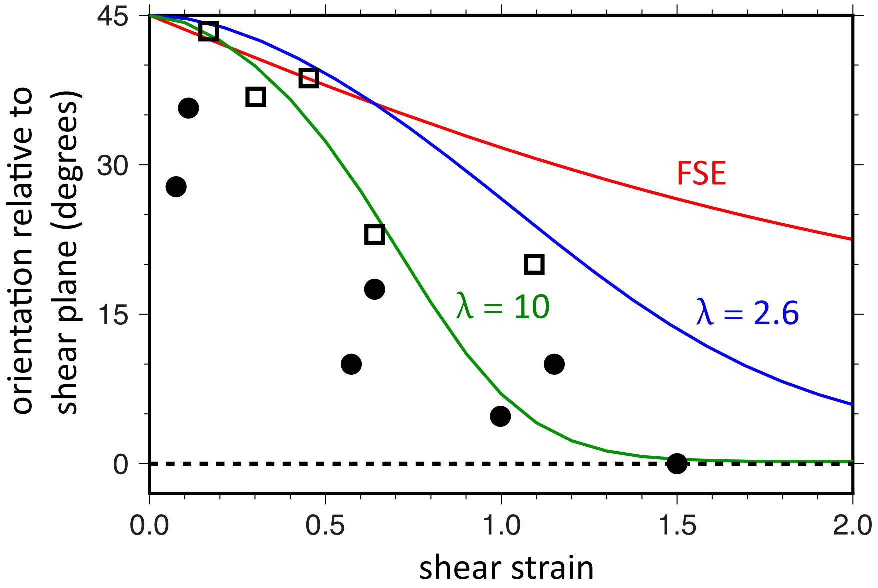

Figure 6. Mean orientation of the [100] axis of olivine as a function of shear strain. Symbols: experiments conducted by S. Zhang & S.I. Karato (1995) at 1473 K (open squares) and 1573 K (filled circles). The line labelled 'FSE' indicates the orientation of the long axis of the finite strain ellipsoid. The other two lines are the expectation values of the [100] orientation predicted by ODFTEX for two different values of the dimensionless recrystallization rate λ.

Because simple shear corresponds to $\Gamma = 1$, the only free parameter in the model is the recrystallization rate λ. To estimate its value, we solve (18) numerically for a range of values of λ and compare the textures in terms of diagnostic parameters such as the M-index (P. Skemer *et al.* 2005), P- and G-scores (F.W. Vollmer 1990) and the mean misfit angle for each of the three crystallographic axes. The results are shown in Fig. A1 of Appendix A. In general, the misfit angle decreases with λ for the a- and b- axes, while it remains constant for the mean c-axis. This is because the modelled c-axes form a girdle around [001], such that the mean c-axis is systematically parallel to this direction. Consistently with previous studies (e.g. Y. Wang *et al.* 2024), the pointness is typically higher than for experimentally deformed samples, indicating that modelled textures tend to overestimate the strength of peaks. Bearing this in mind, with the Euler space discretized in $12^3 = 1728$ elements the best fit to the MIT23 data is obtained for $\lambda = 2.6$, although other values in the range 2.4–3.0 would also give a good fit. As shown in Fig. 5, the model with $\lambda = 2.6$ reproduces the locations of the major peaks in the ODF to within about 10°, and captures the presence of secondary peaks. The model also predicts the observed preferred orientation of the [001] axis about the normal to the plane of deformation, which is not present if recrystallization is inactive (see Fig. 4). Increasing the numerical resolution has the effect of strengthening the fabric. Fig. B1 (Appendix B) shows the texture predicted when dividing the Euler space into $60^3 = 216000$ elements, and is to be compared with the reference case of Fig. 5(b). The M-index is now 0.1334, as opposed to 0.1151 for the reference case, but the general pattern of the texture remains the same. This pattern is consistent with the A-type fabric reproduced in experimental studies (e.g. L.N. Hansen *et al.* 2016), further supporting the validity of our methodology.

5.2.2 Texture and finite strain

How are the textures predicted by ODFTEX related to the orientation of the finite strain ellipsoid (FSE) of the deformation? S. Zhang & S.I. Karato (1995) performed experiments on olivine aggregates deformed in simple shear, and showed that the peak orientation of [100] rotated toward the shear plane much faster than did the long axis of the FSE. S. Zhang & S.I. Karato (1995) interpreted this result as indicating that dynamic recrystallization strongly influenced the observed textures. Fig. 6 shows their measurements of the peak orientation of [100] relative to the shear plane as a function of the shear strain, for experiments conducted at 1473 K (open squares) and 1573 K (filled circles). The red line shows the orientation of the long axis of the FSE. The blue and green lines show the expectation values of the [100] orientation predicted by ODFTEX with $\lambda = 2.6$ and $\lambda = 10$, respectively. In both cases [100] rotates towards the shear plane faster than the FSE does. The curve for $\lambda = 2.6$ provides a better fit to the experimental data at 1473 K, while the curve for $\lambda = 10$ provides a better fit for 1573 K.

6 TEXTURES FORMED UNDER UNIAXIAL COMPRESSION

We now turn to another type of deformation, uniaxial compression, that was commonly used in the early days of experimental rock mechanics before deformation in simple shear was practical. We are fortunate to have available to us a set of 205 crystal orientations measured by A. Nicolas *et al.* (1973) for an experiment in uniaxial compression to 58 per cent shortening. Fig. 7(a) shows the corre-

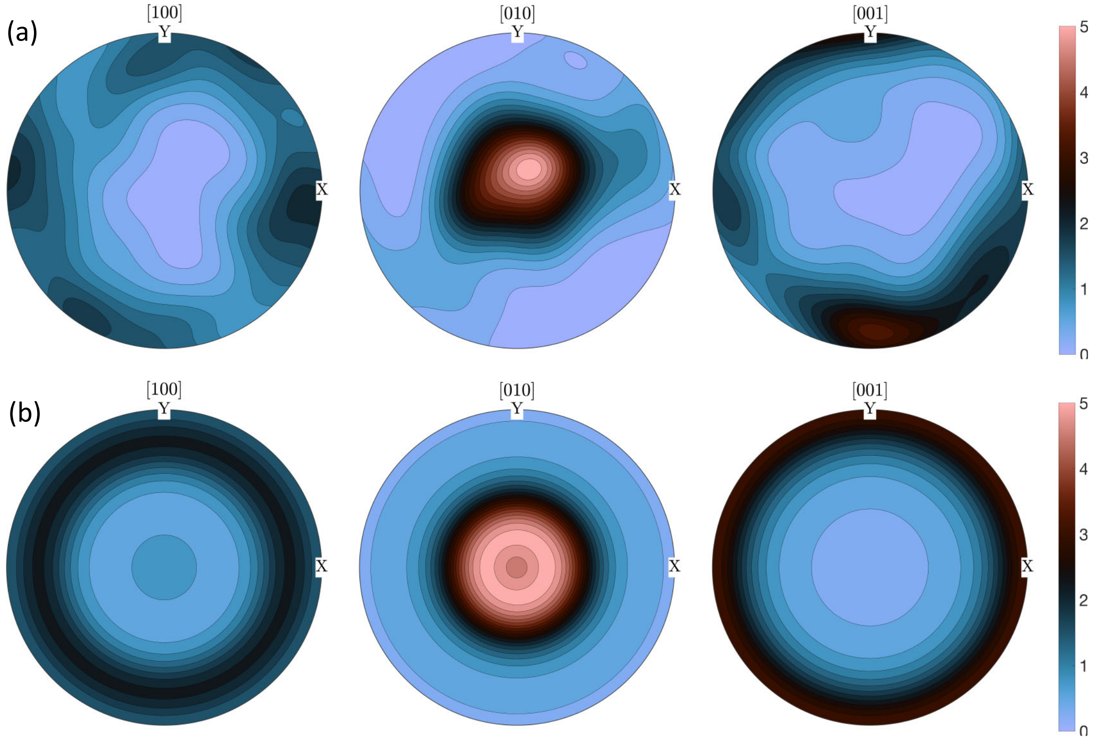

Figure 7. Textures formed under uniaxial shortening of olivine aggregates by 58 per cent. (a) Texture measured in a laboratory experiment (A. Nicolas *et al.* 1973). The compressional axis is at the centre of the pole figures, which were generated using a filter width of 15°. M-index is 0.1302. (b) Texture predicted by ODFTEX with a recrystallization rate $\lambda = 2.6$. M-index is 0.0984. The Euler space was discretized in $12^3 = 1728$ elements for consistency with the filter width used in (a).

sponding pole figures. Fig. 7(b) shows the pole figures predicted by ODFTEX for the same shortening and with a recrystallization rate $\lambda = 2.6$. The agreement between the two textures is remarkable. In both cases the amplitude of the central [010] peak is the same; and the [001] girdle is stronger and more concentrated than the [100] girdle. The fact that ODFTEX can, with the same value of $\lambda = 2.6$, successfully predict textures determined independently for both simple shear and uniaxial compression is strong testimony to the model's utility.

7 TEXTURE EVOLUTION IN COMPLEX FLOW FIELDS

We now show how our approach can be used to predict the evolution of textures in complex, geophysically relevant flow fields. For greater realism, we calculate the texture for a harzburgite aggregate comprising 70 per cent olivine and 30 per cent orthopyroxene. The active slip system in olivine is assumed to be (010)[100] ($s = 1$). Even though the aggregate contains both olivine and orthopyroxene, it is only necessary to solve the evolution eq. (9) once to obtain the master ODF $f(\boldsymbol{g}, t)$. The separate ODFs for olivine and orthopyroxene are then obtained from the master ODF by applying the appropriate rotation matrices $\boldsymbol{M}^{(1)}$ and $\boldsymbol{M}^{(4)}$, as described in Section 2.

7.1 2-D convection model

We first consider an example of plane strain deformation in a 2-D steady convective flow comprising two adjacent cells (8). An isotropic initial condition is imposed at the initial time $t = 0$, and the subsequent evolution of the texture along streamlines is calculated during 20 Ma by solving the evolution eq. (18) using the method of characteristics. The number of elements into which the Euler space is divided is $12 \times 12 \times 12 = 1728$. The dimensionless recrystallization rate is $\lambda = 2.6$. We also implement a texture limiter which causes the amplitude of the texture to saturate above a threshold value of the finite strain. Denoting the three axes of FSE by c_i with $c_1 \geq c_2 \geq c_3$, we stop the evolution of the texture when either $\ln(c_1/c_2)$ or $\ln(c_2/c_3)$ exceeds a value $r_{\max}$, which we here choose to be 5.0. Thereafter the texture rotates passively with the flow. Saturation of texture at large strains has been documented by L.N. Hansen *et al.* (2014) for high-strain torsion experiments.

Fig. 8(c) shows the resulting fields of radial anisotropy (colour) and P-wave anisotropy (white bars). The orientations of the latter closely follow the orientations of the streamlines. For comparison, Fig. 8(b) shows a similar calculation made using D-Rex_M (M. Faccenda *et al.* 2024) with $M^* = 10$, $\chi = 0.3$ and $\lambda^* = 5$. The overall patterns of the ODFTEX and D-Rex predictions are remarkably similar in both orientation and amplitude. As shown in Fig. C1 (Appendix C), the mean angular and P-wave anisotropy deviations are

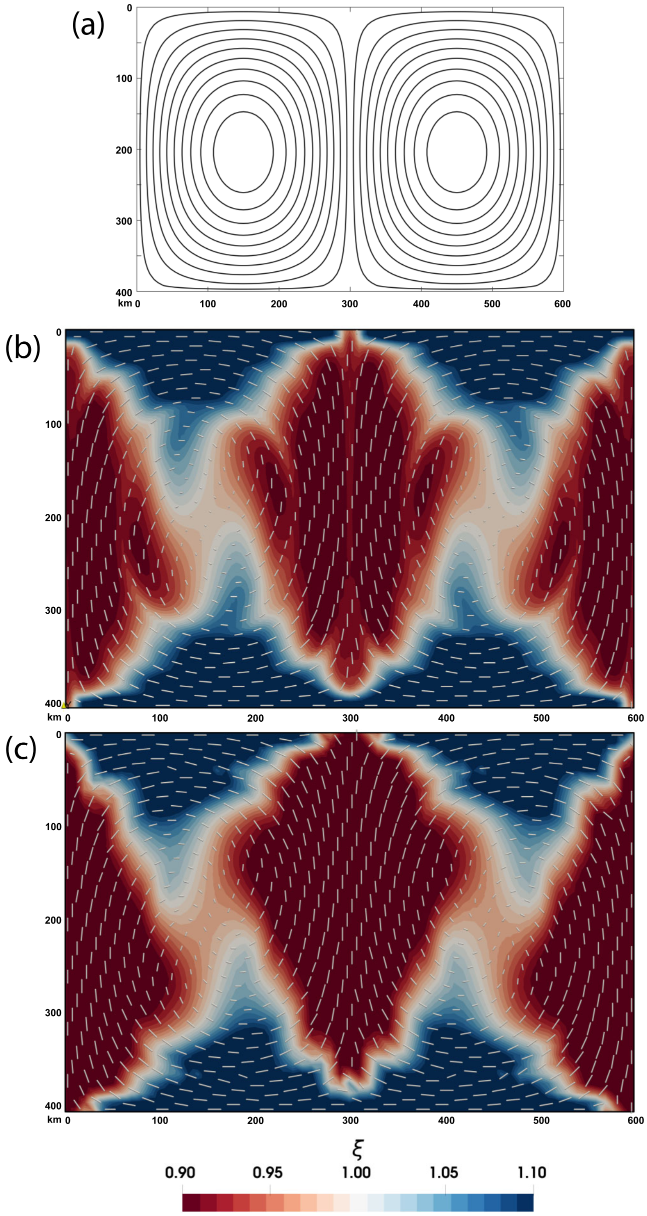

Figure 8. Seismic anisotropy in a kinematically prescribed steady 2-D flow with the streamlines shown in part (a). (b): *S*-wave radial anisotropy (colours) with superimposed *P*-wave fast directions scaled by *P*-wave anisotropy (white bars), calculated using D-Rex_M ($M^* = 10$, $\chi = 0.3$, $\lambda^* = 5$; CRSS: [100](010) = 1; [100](001) = 2, [001](010) = 3, [001](100) = ∞). The evolution of the texture is calculated over 20 Ma starting from an isotropic initial condition, for 9600 harzburgite aggregates (Ol:Opx = 70:30) homogeneously distributed (5 km spacing) over the flow domain. (c). Same as (b), but calculated using ODFTEX with the dominant slip system [100](010), $\lambda = 2.6$ and $r_{\max} = 5$.

$< 10^\circ$ and < 1 per cent, respectively, and the mean difference in radial anisotropy is <0.02. However, the calculation using ODFTEX is about six times faster than the one using D-Rex_M. The general anisotropy pattern is also consistent with those obtained using the SDM (N. Rathmann *et al.* 2024).

7.2 3-D subduction model

Next we use ODFTEX to predict seismic anisotropy in a 3-D, time-dependent flow field induced by oceanic plate subduction in spherical geometry. Because this thermomechanical model has already been presented by M. Faccenda & B. VanderBeek (2023) we give only a brief summary here. The simulation was performed with the I3VIS software (T. Gerya 2019) modified to account for the distortion of the orthogonal grid in spherical coordinates. The numerical domain is $(x_1, x_2, x_3) = (60^\circ - 120^\circ, 5371 - 6371\ \text{km}, 60^\circ - 90^\circ)$, where (x_1, x_2, x_3) are longitude, radius and colatitude. The flow is symmetric with respect to the equatorial plane and only the portion located in the northern hemisphere is modelled. The horizontal portion of the subducting plate is defined in the range $(x_1, x_2, x_3) = (85.4^\circ - 118^\circ, 6281 - 6371\ \text{km}, 80^\circ - 90^\circ)$. A conductive geotherm based on the half-space cooling model (D.L. Turcotte & G. Schubert 2014)

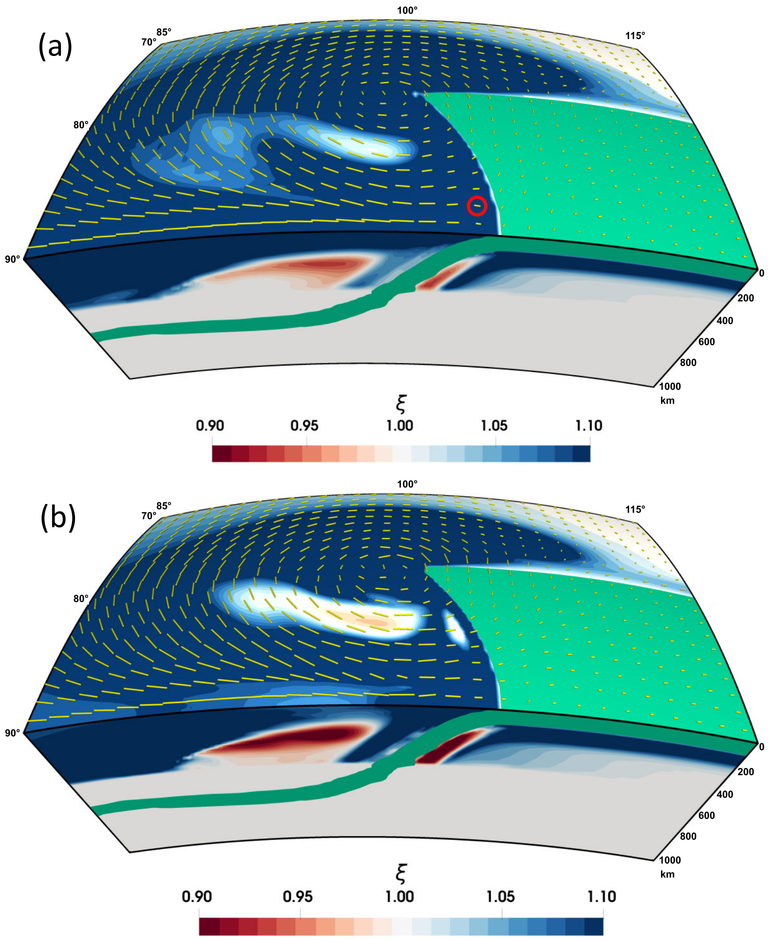

Figure 9. Seismic anisotropy in a 3-D model of oceanic plate subduction calculated using (a) D-Rex and (b) ODFTEX over 19 Ma of model evolution starting from an isotropic initial condition. The model parameters of D-Rex and ODFTEX are the same as in Fig. 8. Colours: *S*-wave radial anisotropy; bars: SKS fast azimuths scaled by delay time [1.76 s for the bar inside the red circle in part (a)]. The volume in green encloses material with a $+1$ per cent isotropic *P*-wave anomaly (i.e. the oceanic plate). The apparently thicker slab portion around the 410 km depth discontinuity is due to the upwelling of the olivine-spinel phase transition. Elastic properties were computed for 767064 mantle aggregates homogeneously distributed (20 km spacing) within the $(x_1, x_2, x_3) = (85^\circ\text{–}115^\circ,\ 5371\text{–}6371\ \text{km},\ 70^\circ\text{–}90^\circ)$ domain.

is imposed in the uppermost 90 km thick layer, while an adiabatic gradient of 0.5 K km^{-1} is imposed in the underlying convective mantle. The plate age varies from 80 to 40 Myr from the centre to the edge of the plate, which favours the formation of a curved trench (G. Morra *et al.* 2006) and decreases linearly to 1 Myr at $(x_1) = (118^\circ - 119^\circ)$ to prevent subduction at the trailing edge. The background plate age is set to 1 Myr to minimize mechanical interaction with and favour subduction of the old plate. Self-consistent subduction is initiated by the imposition of a 200 km long protoslab and is lubricated by a 15 km thick crustal layer with weak brittle behaviour. The rheological model accounts for viscoplastic deformation. Viscous behaviour results from combined low-T (Peierls) and high-T (diffusion and dislocation) creep mechanisms. The viscosity of the lower mantle is increased by a factor 30, which favours slab stagnation in the mantle transition zone.

The model evolution is characterized by plate subduction and retreat accommodated by lateral toroidal flow, and by plate stagnation in the mantle transition zone. The evolution of upper mantle textures is computed assuming that all the deformation is accommodated by dislocation creep, which yields upper bound estimates for the strength of the CPOs and related anisotropy. Fig. 9 shows the *S*-wave radial anisotropy (colours) and SKS splitting vectors (gold bars) for upper mantle fabrics calculated using (a) D-Rex and (b) ODFTEX, using the same model parameters as in Fig. 8. The predictions of the two simulations are quite similar, as shown quantitatively in Fig. C2 (Appendix C). The mean azimuthal and delay time deviations of the SKS splitting patterns are $< 10^\circ$ and 0.2 s, respectively, and the mean difference in radial anisotropy is 0.003. The toroidal component of the flow favours the generation of horizontal fabrics and positive radial anisotropy, while subvertical fabrics and negative radial anisotropy are caused by poloidal currents. Synthetic SKS splitting patterns computed using the matrix propagation method described in G. Rümpker & P. Silver (1998) are characterized by fast azimuths that are trench-normal around the trench and mantle wedge areas and progressively orient parallel to the toroidal flow at depth toward the edge of the subduction zone. Both simulations delineate clear toroidal vortices around the plate's lateral edge. Again, we find that ODFTEX outpaces D-Rex by a factor of 6.5.

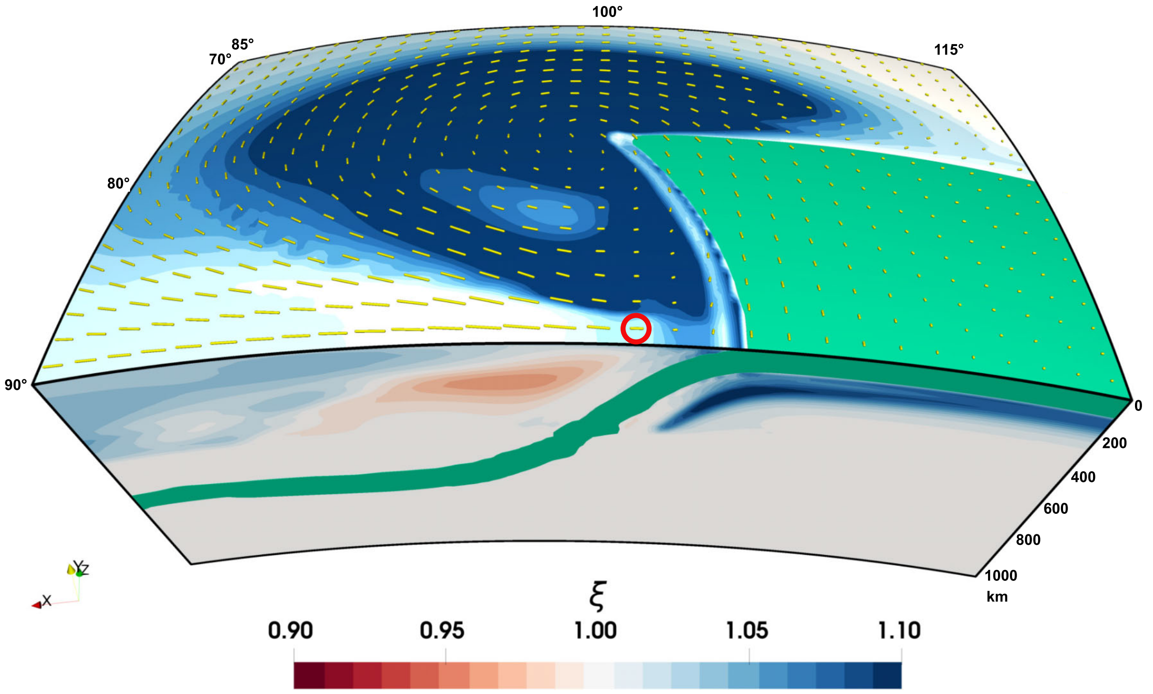

Figure 10. Same as Fig. 9, but for $\lambda = 0$ (no recrystallization). SKS fast azimuths are scaled by delay time (2.38 s for the bar inside the circle).

Fig. 10 is the same as Fig. 9(b) except that $\lambda = 0$ (no recrystallization). The anisotropy is now weaker overall. In addition, the SKS splitting no longer delineates a clear toroidal vortex, and the fast directions are now subparallel to the trench in the forearc and seaward of the trench.

The modelled fabrics and SKS splitting patterns are qualitatively consistent with those associated with retreating subduction models in Cartesian coordinates that employed D-Rex (M. Faccenda & F.A. Capitanio 2013; J.P. Kruse *et al.* 2024), and by J. Di Leo *et al.* (2014), who used the VPSC model. Because of different slab dynamics (retreating versus advancing), it is more difficult to compare our results with the subduction models of M. Fraters & M. Billen (2021), which employed D-Rex, and of Y. Wang *et al.* (2024) and Y. Wang *et al.* (2025), who in addition tested the MDM with anisotropic viscosity. Nevertheless, a clear similarity exists among the fabrics of the subslab crystal aggregates, which experience simple shear deformation in all the different studies.

8 DISCUSSION

The model we have presented here has two main novel features. The first is a continuous representation of the texture in terms of the ODF, as opposed to a discrete representation in terms of individual grains. The ODF is obtained directly by solving a hyperbolic evolution equation numerically along pathlines in the flow, making it unnecessary to determine it from grain orientations via an inherently non-unique smoothing procedure. The use of the ODF evolution equation leads directly to the second novel aspect of our approach: a recrystallization model that takes the form of an inhomogeneous term on the right-hand side of the equation. Our recrystallization model is agnostic in the sense that it makes no hypotheses about the microscopic mechanisms by which dynamic recrystallization occurs. Instead, we assume only that recrystallization is faster for grains that are poorly oriented for slip, which allows us to describe the process with only a single free parameter, the dimensionless recrystallization rate λ. This purely kinematic approach differs essentially from D-Rex (E. Kaminski *et al.* 2004), which attempts to quantify the mechanisms underlying dynamic recrystallization. The result is that D-Rex has three independent free parameters, while ODFTEX has only one. With $\lambda = 2.6$, our new model fits experimental pole figure data as well as does D-Rex, even with the latter's greater number of fitting parameters.

An independent way to constrain the value of λ is to use data on the orientation of the [100] axis as a function of strain in simple shear. Fig. 6 shows the [100] orientation data from experiments at 1473 K (open squares) and 1573 K (solid circles) from S. Zhang & S.I. Karato (1995) together with the predictions of ODFTEX for $\lambda = 2.6$ and 10. The choice $\lambda = 2.6$ gives a better fit to the data at 1473 K, while $\lambda = 10$ gives a better fit for 1573 K. However, the data of S. Zhang & S.I. Karato (1995) are highly scattered and presumably have large error bars (not given in their paper). We therefore prefer to constrain λ by comparing our model predictions with the complete pole figures of Fig. 5, which contain much more information than simple [100] orientations. In summary, we recommend that eventual users of our model choose the value $\lambda = 2.6$.

In modelling the plastic deformation of olivine, we have assumed that only a single dominant slip system need be taken into account. This simplifies the theory substantially and reduces the computational cost of the numerical implementation. This assumption

Table 1. Symbols used.

Symbol	Meaning	Units
$\boldsymbol{a}$	direction cosine matrix	none
$\boldsymbol{b}$	Burgers vector	none
$e_{ij} \equiv \dot{\gamma} S_{ij}$	crystal strain rate tensor	s^{-1}
E_{ij}	global strain rate tensor	s^{-1}
$\mathcal{E} \equiv (e_{ij} - E_{ij})(e_{ij} - E_{ij})$	strain rate misfit	s^{-2}
f	orientation distribution function	none
$\mathbf{g} \equiv (\phi, \theta, \psi)$	crystal orientation	none
$\dot{\mathbf{g}}$	crystallographic spin	s^{-1}
$\dot{\mathbf{g}}_e$	extrinsic spin	s^{-1}
$\hat{f}$	recrystallization rate function	s^{-1}
$\boldsymbol{M}^{(s)}$	rotation matrix for slip system s	none
$\boldsymbol{n}$	normal to slip plane	none
r_{max}	maximum logarithmic strain	none
$S_{ij} \equiv \frac{1}{2}(n_i b_j + n_j b_i)$	Schmid tensor	none
t	time	s
$\dot{\gamma}$	slip rate on slip system	s^{-1}
$\Gamma \equiv \dot{\Omega}/\dot{\epsilon}_0$	vorticity number for plane strain	none
$\dot{\epsilon}_0 \equiv \sqrt{E_{ij}E_{ij}/2}$	strain rate scale	s^{-1}
θ_e, ϕ_e	spherical coordinates of extrinsic spin vector	none
$\lambda \equiv \Lambda/\dot{\epsilon}_0$	dimensionless recrystallization rate	none
Λ	recrystallization rate	s^{-1}
$\tau \equiv \dot{\epsilon}_0 t$	dimensionless time	none
ϕ, θ, ψ	Eulerian angles	none
$\dot{\psi} \equiv S_{ij}E_{ij}$	crystallographic spin	s^{-1}
$\dot{\Psi} \equiv \dot{\psi}/\dot{\epsilon}_0$	dimensionless crystallographic spin	none
$\dot{\Omega}$	extrinsic spin in plane strain	s^{-1}
$\dot{\Omega}_i$	Cartesian components of extrinsic spin	s^{-1}

Table 2. Comparison of the ODFTEX, D-Rex and SOSC models. Green, orange and red squares indicate that the characteristic indicated fully pertains, partly pertains or does not pertain, respectively, to the model in question.

Characteristic	ODFTEX	D-Rex	SOSC
Delivers the ODF directly	🟩	🟥	🟥
Avoids excessively sharp textures	🟩	🟧	🟥
Fast enough for time-dependent flow fields	🟩	🟧	🟥
Orthopyroxene included	🟩	🟩	🟩
Recrystallization model with few parameters	🟩	🟧	🟥
Arbitrary initial condition allowed	🟩	🟩	🟩
Multiple slip systems possible	🟥	🟩	🟩
Relative cost	1	$6-7$	10^6

is supported by the fact that a model with only a single active slip system (010)[100] and a suitably chosen recrystallization rate $\lambda = 2.6$ matches remarkably well the results of two independent laboratory experiments: in simple shear (K.H. Lee *et al.* 2002) and in uniaxial compression (A. Nicolas *et al.* 1973). However, our assumption will not be valid if the critical resolved shear stresses (CRSSs) of the weakest and next-to-weakest slip systems are close to one another. J. Signorelli *et al.* (2021) assume that the CRSSs for (010)[100] and (001)[100] are identical, without however citing a source. L. Mameri *et al.* (2019) assume that the normalized CRSSs for (010)[100], (001)[100] and (010)[001] are 1, 1.5 and 2, respectively, again without citing a source. Since the rate of slip on a slip system is proportional to CRSS^{-n}, where $n = 3.5$ is the power-law exponent of the slip system rheology (Q. Bai *et al.* 1991), the activity of (001)[100] in L. Mameri *et al.* (2019) would be 24 per cent of that of (010)[100]. However, the truth is that we simply do not know (and will probably never know) the relative values of the CRSSs for olivine under mantle conditions. Given the state of our ignorance, models assuming a single dominant slip system [e.g. ODFTEX and the SDM of N. Rathmann *et al.* (2024)] do not seem unreasonable. However, we readily acknowledge that such models will not be able to reproduce more complex textures such as the AG-type fabric characterized by girdles of [100] and [001] parallel to the shear plane, which are likely produced by the similar and competing activities of the (010)[100] and (010)[001] slip systems. For such cases the D-Rex model remains available for use.

Table 2 gives a schematic comparison of ODFTEX with the D-Rex and SOSC models. The green, orange and red squares indicate that the model in question fully satisfies, partially satisfies and does not satisfy, respectively, the criterion indicated. Of the three models, ODFTEX is the only one that delivers the ODF directly. Next, ODFTEX includes a mechanism that limits the amplitude of the texture at large strains, a criterion that is only partly satisfied by D-Rex and is not at all satisfied by SOSC. Furthermore, ODFTEX is the model best adapted for use in complex time-dependent flows. ODFTEX allows the effect of orthopyroxene to be included, as do the other two models. ODFTEX also has a recrystallization model with only a single parameter, whereas D-Rex has three parameters and SOSC has no recrystallization model. All three models allow calculation of texture starting from an arbitrary initial condition. Finally, ODFTEX is the least expensive of the three models, being about 6.5 times faster than D-Rex and 10^6 times faster than SOSC.

ACKNOWLEDGMENTS

We are grateful to R. Hielscher for proposing and testing an explanation for why textures due to a single active slip system without recrystallization always have one isotropic and two non-isotropic pole figures. We thank S.-i. Karato for providing the crystal orientation data from the MIT23 experiment, and F. Boudier and the late A. Nicolas for providing data from the uniaxial compression experiment of A. Nicolas *et al.* (1973). We also thank Agnes Király and an anonymous reviewer for many constructive comments that helped us greatly to improve the original manuscript. NMR was supported by the Horizon Europe ERC Grant No. 101098375 SOFT-PLANET. MF was supported by the Horizon 2020 ERC Grant No. 758199 NEWTON.

DATA AVAILABILITY

The software for reproducing the data presented in this study is available at https://github.com/mfaccenda/ECOMAN3.0⟨plxhyp⟩PLXHYP⟨/plxhyp⟩geodynamics.Beta. Instructions to compile and run the codes are provided in README_Instructions.pdf. Pole figures were plotted using the berlin colourmap from F. Crameri (2023).

REFERENCES

Bai, Q., Mackwell, S.J. & Kohlstedt, D.L., 1991. High-temperature creep of olivine single crystals, 1. Mechanical results for buffered samples, *J. geophys. Res.,* **96,** 2441–2463.

Becker, T.W., Kustowski, B. & Ekström, G., 2008. Radial seismic anisotropy as a constraint for upper mantle rheology, *Earth planet. Sci. Lett.,* **267,** 213–227.

Blackman, D.K. & Kendall, J.M., 2002. Seismic anisotropy in the upper mantle 2. Predictions for current plate boundary flow models, *Geochem. Geophys. Geosyst.,* **3,** 8602.

Castelnau, O., Blackman, D.K., Lebensohn, R.A. & Castañeda, P.P., 2008. Micromechanical modeling of the viscoplastic behavior of olivine, *J. geophys. Res.,* **113,** B09202.

Clement, A., 1982. Prediction of deformation texture using a physical principle of conservation, *Mater. Sci. Eng.,* **55,** 203–210.

Conder, J.A. & Wiens, D.A., 2007. Rapid mantle flow beneath the Tonga volcanic arc, *Earth planet. Sci. Lett.,* **264,** 299–307.

Crameri, F., 2023. Scientific colour maps.1243862.

Di Leo, J., Walker, A., Li, Z.H., Wookey, J., Ribe, N., Kendall, J.M. & Tommasi, A., 2014. Development of texture and seismic anisotropy during the onset of subduction, *Geochem. Geophys. Geosyst.,* **15,** 192–212.

Etchecopar, A. & Vasseur, G., 1987. A 3-D kinematic model of fabric development in polycrystalline aggregates: comparisons with experimental and natural samples, *J. Struct. Geol.,* **9,** 705–717.

Faccenda, M. & Capitanio, F.A., 2013. Seismic anisotropy around subduction zones: Insights from three-dimensional modeling of upper mantle deformation and SKS splitting calculations, *Geochem. Geophys. Geosyst.,* **14,** 243–262.

Faccenda, M. & VanderBeek, B., 2023. On constraining 3d seismic anisotropy in subduction, mid-ocean-ridge, and plume environments with teleseismic body wave data, *J. Geodyn.,* **158,** 102003.

Faccenda, M., VanderBeek, B.P., de Montserrat, A., Yang, J., Rappisi, F. & Ribe, N., 2024. Ecoman: an open-source package for geodynamic and seismological modelling of mechanical anisotropy, *Solid Earth,* **15**(10), 1241–1264.

Fraters, M. & Billen, M., 2021. On the implementation and usability of crystal preferred orientation evolution in geodynamic modeling, *Geochem. Geophys. Geosyst.,* **22,** e2021GC009846.

Gerya, T., 2019. *Introduction to numerical geodynamic modelling, 358 pp.,* Cambridge: Cambridge University Press.

Goulding, N., Ribe, N., Castelnau, O., Walker, A.M. & Wookey, J., 2015. Analytical parametrization of self-consistent polycrystal mechanics: Fast calculation of upper mantle anisotropy, *Geophys. J. Int.,* **203,** 334–350.

Hall, C.E., Fischer, K.M., Parmentier, E.M. & Blackman, D.K., 2000. The influence of plate motions on three-dimensional back arc mantle flow and shear wave splitting, *J. geophys. Res.,* **105,** 28009–28033.

Hansen, L.N., Zhao, Y.H., Zimmerman, M.E. & Kohlstedt, D.L., 2014. Protracted fabric evolution in olivine: Implications for the relationship among strain, crystallographic fabric, and seismic anisotropy, *Earth planet. Sci. Lett.,* **387,** 157–168.

Hansen, L.N., Conrad, C.P., Boneh, Y., Skemer, P., Warren, J.M. & Kohlstedt, D.L., 2016. Viscous anisotropy of textured olivine aggregates: 2. micromechanical model, *J. geophys. Res. Solid Earth,* **121,** 7137–7160.

Jung, H., Katayama, I., Jiang, Z., Hiraga, T. & Karato, S.I., 2006. Effect of water and stress on the lattice-preferred orientation of olivine, *Tectonophys.,* **421,** 1–22.

Kaminski, E. & Ribe, N., 2001. A kinematic model for recrystallization and texture development in olivine polycrystals, *Earth planet. Sci. Lett.,* **189,** 253–267.

Kaminski, E., Ribe, N.M. & Browaeys, J.T., 2004. D-Rex, a program for calculation of seismic anisotropy in the convective upper mantle, *Geophys. J. Int.,* **158,** 744–752.

Karato, S.I., Jung, H., Katayama, I. & Skemer, P., 2008. Geodynamic significance of seismic anisotropy of the upper mantle: New in- sights from laboratory studies, *Annu. Rev. Earth Planet. Sci.,* **36,** 59–95.

Király, A., Conrad, C.P. & Hansen, L.N., 2020. Evolving viscous anisotropy in the upper mantle and its geodynamic implications, *Geochem. Geophys. Geosyst.,* **21,** e2020GC00915.

Kruse, J.P., Rümpker, G., Link, F., Duretz, T. & Schmeling, H., 2024. Anisotropy and xks splitting from geodynamic models of double subduction: testing the limits of interpretation, *Geophys. J. Int.,* **239**(3), 1400–1424.

Lassak, T.M., Fouch, M.J., Hall, C.E. & Kaminski, E., 2006. Seismic characterization of mantle flow in subduction systems: Can we resolve a hydrated mantle wedge?, *Earth planet. Sci. Lett.,* **243,** 632–649.

Lebensohn, R.A., 2001. N-site modeling of a 3D viscoplastic polycrystal using fast Fourier transform, *Acta Mater.,* **49,** 2723–2737.

Lebensohn, R.A. & Tomé, C.N., 1993. A self-consistent anisotropic approach for the simulation of plastic deformation and texture development of polycrystals: Application to zirconium alloys, *Acta Metall. Mater.,* **41,** 2611–2624.

Lebensohn, R.A., Liu, Y. & Ponte Castañeda, P., 2004a. Macroscopic properties and field fluctuations in model power-law polycrystals: Full-field solutions versus self-consistent estimates, *Proc. R. Soc. Lond. A,* **460,** 1381–1405.

Lebensohn, R.A., Liu, Y. & Ponte Castañeda, P., 2004b. On the accuracy of the self-consistent approximation for polycrystals: comparison with full-field numerical simulations, *Acta Mater.,* **52,** 5347–5361.

Lebensohn, R.A., Ponte Castañeda, P., Brenner, R. & Castelnau, O., 2011. Full-field vs. homogenization methods to predict microstructure-property relations for polycrystalline materials, in *Computational Methods for Microstructure-Property Relationships,* chap. 11, pp. 393–442, eds Ghosh, S. & Dimiduk, D., Springer.

Lee, K.H., Jiang, Z. & Karato, S.I., 2002. A scanning electron microscope study of the effects of dynamic recrystallization on lattice preferred orientation in olivine, *Tectonophys.,* **351,** 331–341.

Lev, E. & Hager, B.H., 2008. Prediction of anisotropy from flow models: a comparison of three methods, *Geochem. Geophys. Geosyst.,* **9,** Q07014.

Li, Z.H., Di Leo, J.F. & Ribe, N.M., 2014. Subduction-induced mantle flow, finite strain, and seismic anisotropy: Numerical modeling, *J. geophys. Res. Solid Earth,* **119,** 5052–5076.

Liu, Y. & Ponte Castañeda, P., 2004. Second-order theory for the effective behavior and field fluctuations in viscoplastic polycrystals, *J. Mech. Phys. Solids,* **52,** 467–495.

Long, M.D. & Becker, T.W., 2010. Mantle dynamics and seismic anisotropy, *Earth planet. Sci. Lett.,* **297,** 341–354.

Long, M.D., Hager, B.H., de Hoop, M.V. & van der Hilst, R.D., 2007. Two-dimensional modelling of subduction zone anisotropy with application to southwestern Japan, *Geophys. J. Int.,* **170,** 839–856.

Mameri, L., Tommasi, A., Signorelli, J. & Hansen, L.N., 2019. Predicting viscoplastic anisotropy in the upper mantle: a comparison between experiments and polycrystal plasticity models, *Phys. Earth planet. Int.,* **286,** 69–80.

McKenzie, D., 1979. Finite deformation during fluid flow, *Geophys. J. R. astr. Soc.,* **58,** 689–715.

Molinari, A., Canova, G.R. & Ahzi, S., 1987. A self-consistent approach of the large deformation polycrystal viscoplasticity, *Acta Metall. Mater.,* **35,** 2983–2994.

Montagner, J.P. & Guillot, L., 2002. Seismic anisotropy and global geodynamics, *Rev. Mineral. Geochem.,* **51,** 353–385.

Morra, G., Regenauer-Lieb, K. & Giardini, D., 2006. Curvature of island arcs, *Geology,* **34,** 877–880.

Moulinec, H. & Suquet, P., 1998. A numerical method for computing the overall response of nonlinear composites with complex microstructure, *Comput. Methods Appl. Mech. Eng.,* **157,** 69–94.

Mühlhaus, H., Moresi, L., Hobbs, B. & Dufour, F., 2002. Large amplitude folding in finely layered viscoelastic rock structures, *Pure appl. Geophys.,* **159,** 2311–2333.

Mühlhaus, H.B., Moresi, L. & Cada, M., 2004. Emergent anisotropy and flow alignment in viscous rock, *Pure appl. Geophys.,* **161,** 2451–2463.

Nicolas, A., Boudier, F. & Boullier, A.M., 1973. Mechanisms of flow in naturally and experimentally deformed peridotites, *Am. J. Sci.,* **273,** 853–876.

Phipps Morgan, J., 1987. Melt migration beneath mid-ocean spreading centers, *Geophys. Res. Lett.,* **14,** 1238–1241.

Ponte Castañeda, P., 2002. Second-order homogenization estimates for nonlinear composites incorporating field fluctuations: I-theory, *J. Mech. Phys. Solids,* **50,** 737–757.

Rathmann, N., Mosegaard, K., Bekkevold, I., Lilien, D. & Prior, D., 2024. A spectral directors method for modeling the coupled evolution of flow and cpo in polycrystalline olivine, *Geochem. Geophys. Geosyst.,* **25,** e2024GC011831.

Ribe, N.M., 1992. On the relation between seismic anisotropy and finite strain, *J. geophys. Res.,* **97,** 8737–8747.

Ribe, N.M. & Yu, Y., 1991. A theory for plastic deformation and textural evolution of olivine polycrystals, *J. geophys. Res.,* **96,** 8325–8335.

Ribe, N.M., Hielscher, R. & Castelnau, O., 2019. An analytical finite-strain parametrization for texture evolution in deforming olivine polycrystals, *Geophys. J. Int.,* **216,** 486–514.

Rümpker, G. & Silver, P., 1998. Apparent shear-wave splitting parameters in the presence of vertically varying anisotropy, *Geophys. J. Int.,* **135**(3), 790–800.

Sarma, G.B. & Dawson, P.R., 1996. Effects of interactions among crystals on the inhomogeneous deformation of polycrystals, *Acta Mater.,* **44,** 1937–1953.

Signorelli, J. & Tommasi, A., 2015. Modeling the effect of subgrain rotation recrystallization on the evolution of olivine crystal preferred orientations in simple shear, *Earth planet. Sci. Lett.,* **430,** 356–366.

Signorelli, J., Hassani, R., Tommasi, A. & Mameri, L., 2021. An effective parameterization of texture-induced viscous anisotropy in orthotropic materials with application for modeling geodynamical flows, *J. Theor. Comp. Appl. Mech.,* **Jul 13, 2021,** 1–17.

Silver, P.G. & Chan, W.W., 1991. Shear wave splitting and subcontinental mantle deformation, *J. geophys. Res.,* **96,** 16429–16454.

Skemer, P., Katayama, I., Jiang, Z. & Karato, S.I., 2005. The misorientation index: development of a new method for calculating the strength of lattice-preferred orientation, *Tectonophys.,* **411,** 157–167.

Tommasi, A., 1998. Forward modeling of the development of seismic anisotropy in the upper mantle, *Earth planet. Sci. Lett.,* **160,** 1–13.

Turcotte, D.L. & Schubert, G., 2014. *Geodynamics,* Cambridge: Cambridge Univ. Press, 3rd edn.

Vollmer, F.W., 1990. An application of eigenvalue methods to structural domain analysis, *Geol. Soc. Am. Bull.,* **102,** 786–791.

Wang, Y., Kiraly, A., Conrad, C.P., Hansen, L. & Fraters, M., 2024. The importance of anisotropic viscosity in numerical models, for olivine textures in shear and subduction deformations, *Tektonika,* **2.1,** 157–173.

Wang, Y., Király, A., Conrad, C.P. & Maupin, V., 2025. Mantle flow and anisotropy in subduction zones: modeling and clustering of olivine textures, *Geochem. Geophys. Geosyst.,* **26,** e2025GC012160.

Wenk, H.R. & Tomé, C.N., 1999. Modelling dynamic recrystallization of olivine aggregates deformed in simple shear, *J. geophys. Res.,* **104,** 25513–25527.

Wenk, H.R., Bennett, K., Canova, G.R. & Molinari, A., 1991. Modelling plastic deformation of peridotite with the self-consistent theory, *J. geophys. Res. Solid Earth,* **96,** 8337–8349.

Zhang, S. & Karato, S.I., 1995. Lattice preferred orientation of olivine aggregates deformed in simple shear, *Nature,* **375,** 774–777.

APPENDIX A: QUANTITATIVE COMPARISON OF MODEL PREDICTIONS WITH EXPERIMENTAL DATA FOR SIMPLE SHEAR

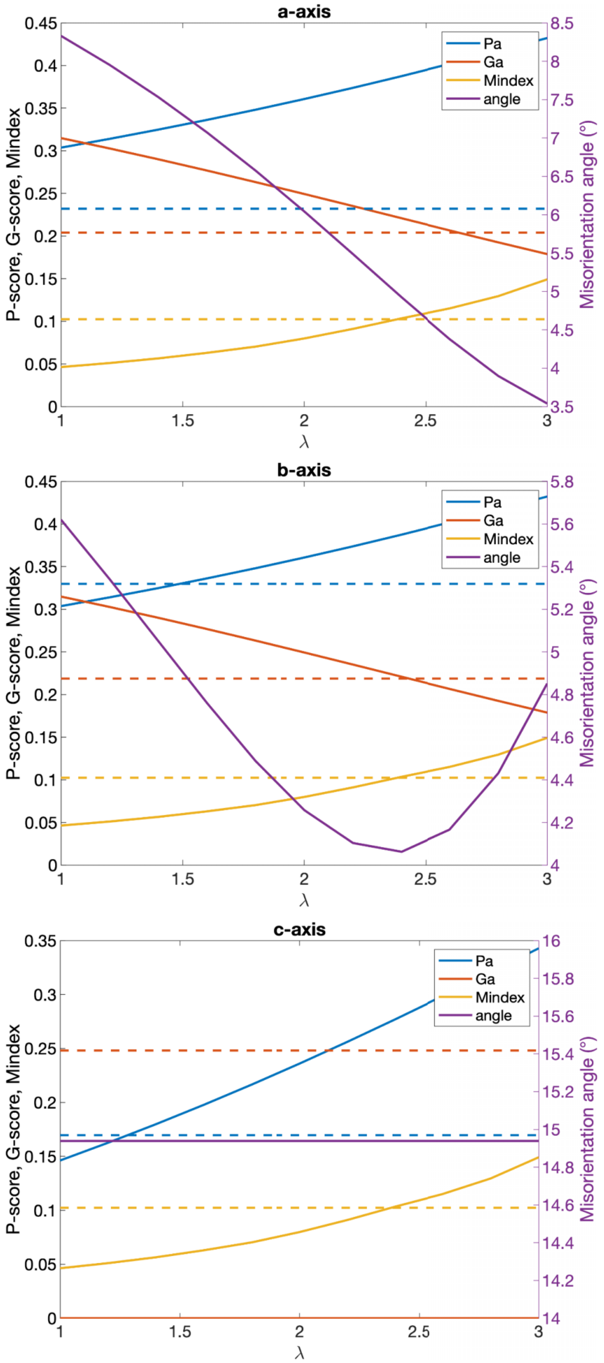

Figure A1. Comparison of model predictions as a function of the recrystallization rate λ with observations from sample MIT23 from K.H. Lee *et al.* (2002). Model textures are generated for simple shear to 140 per cent shear strain. The comparison is performed by employing several diagnostic parameters for each of the three crystallographic axes: the M-index, the pointness P and the girdleness G (left vertical axis). Dashed lines are the corresponding parameters for the sample MIT23. The purple curves indicate misorentation angles of the mean orientations of the axes.

APPENDIX B: EFFECT ON ODFTEX PREDICTIONS OF INCREASING RESOLUTION

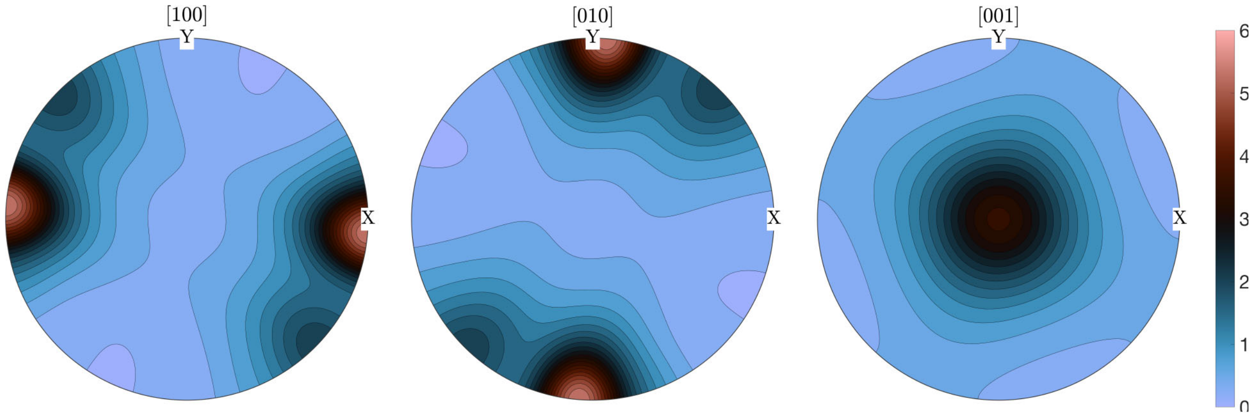

Figure B1. Same as Fig. 5(b), but with the Euler space discretized in $60^3 = 216000$ elements.

APPENDIX C: COMPARISON OF D-REX AND ODFTEX MODEL PREDICTIONS FOR 2-D AND 3-D FLOW MODELS

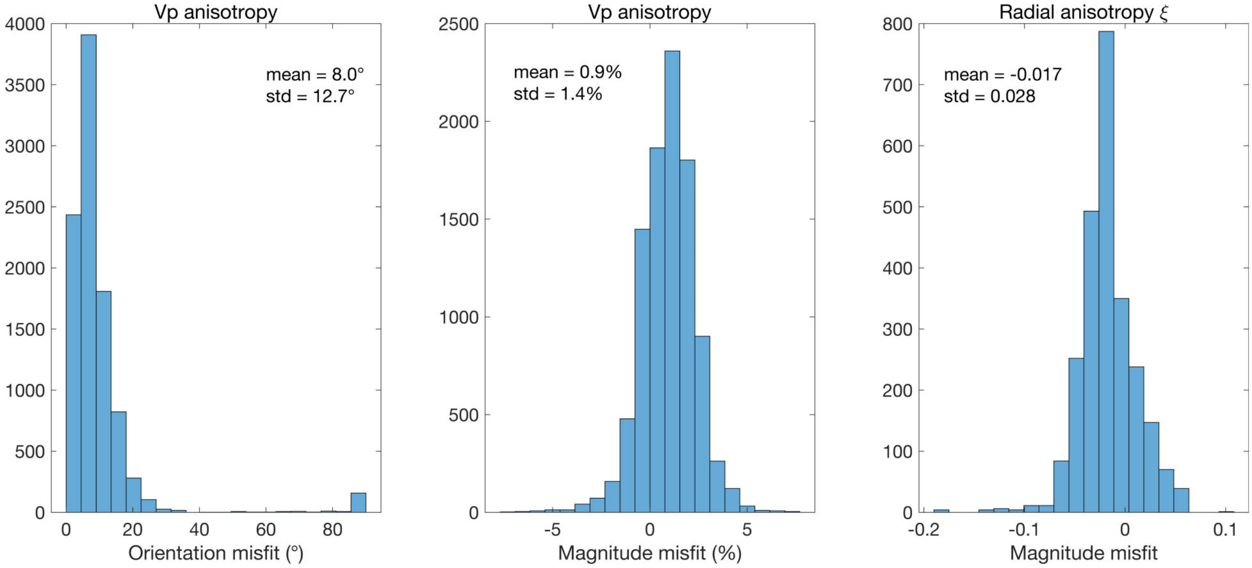

Figure C1. Deviations in *P*-wave anisotropy (left and centre) and radial anisotropy (right) for the predictions of the D-Rex and ODFTEX texture models shown in Fig. 8. Angular deviations are the minimum angle formed by the fast *P*-wave direction vectors, while differences in magnitude of the *P*-wave and radial anisotropy are computed by subtracting the D-Rex model values from the ODFTEX ones.

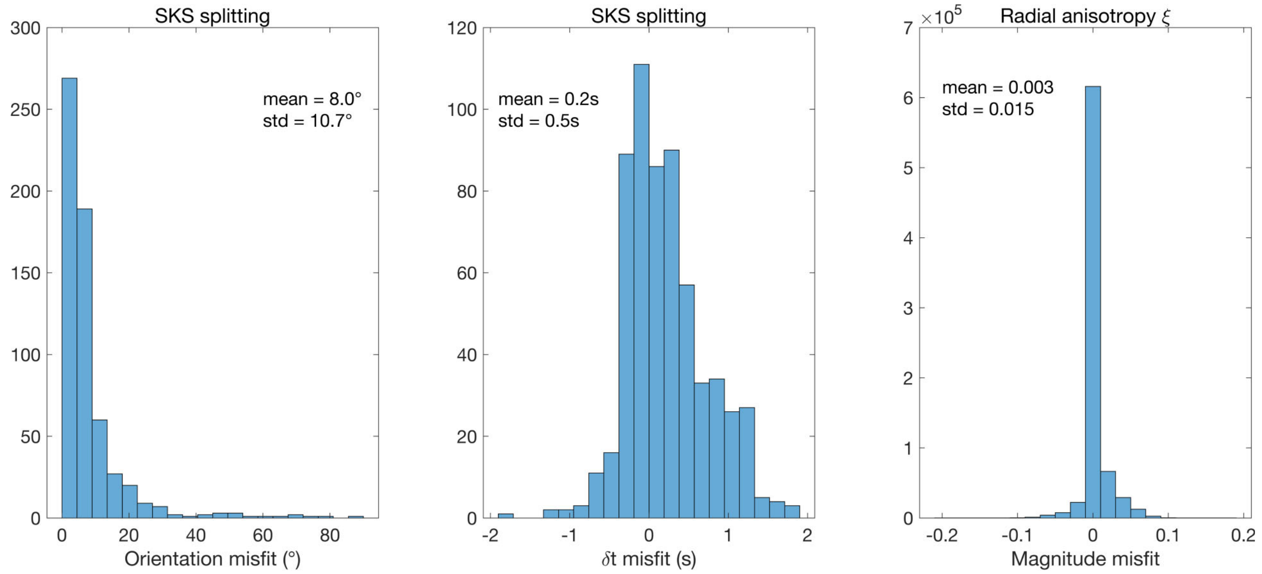

Figure C2. Deviations in SKS splitting anisotropy (left and centre) and radial anisotropy (right) for the predictions of the D-Rex and ODFTEX texture models shown in Fig. 9. Angular deviations are the minimum angle formed by the fast *P*-wave direction vectors, while differences in magnitude of the *P*-wave and radial anisotropy are computed by subtracting the D-Rex model values from the ODFTEX ones.